Eidgenössische Technische Hochschule Zürich
Swiss Federal Institute of Technology Zurich

Institute for Biomedical Engineering
Cardiovascular Magnetic Resonance
Semester Project Spring 2017

Semester Project

Alen Mujkanović

Compressed Sensing Reconstruction for MR Elastography: Towards Free-Breathing MRE

Supervisors: Christian Günthner
Sebastian Kozerke

Abstract

In clinical practice, Magnetic Resonance Elastography (MRE) is most commonly employed to assess the progression of hepatic fibrosis (1). During a typical MRE screening, the patients are instructed to suspend breathing after exhalation for periods of $10 - 20s$ to minimize the effects of respiratory motion on the reconstruction outcome (2). To enable free-breathing MRE, we investigate the application of compressed sensing image reconstruction techniques, specifically adaptations of XD-GRASP (3) and Low-rank plus Sparse (4), which have previously been used with free-breathing abdominal imaging and DCE-MRI. Evaluation of reconstruction with varying parameters and sparsifying transformations was performed on *in silico* acquisitions from measured phantom data. In the defined motion bins, best results show $2 - 3\%$ deviation from ground truth values in reconstructed elastograms for fivefold undersampled motion-resolved data. These results were attained through simultaneous regularization using two sparsifying transformations: 1) the Fourier transform along the wave phase of the externally introduced shear wave, and 2) total variation across respiratory motion states. The evaluation indicates that results comparable to established breath-hold MRE techniques can potentially be attained by navigator-based free-breathing implementations using the proposed reconstruction scheme, but remains to be demonstrated *in vivo*.

Introduction

The mechanical properties of tissues in the human body are affected by a wide array of medical conditions. Methods for determining and comparing tissue stiffness have long been in clinical use. Simple palpation can be a useful method for physicians to discover superficial lesions, such as breast tumors, and is also applicable inside the body during open surgery. Quantitative measurements on the surface can be assessed by mechanical palpation devices (5), or compression optical coherence elastography (OCE) (6). However, there is also a need to characterize tissues deep inside the body, such as the liver, which is commonly affected by fibrosis in response to chronic damage (1,7), or tumors of abdominal organs. Determining the stiffness and viscoelastic properties of tissues in a non-invasive and quantitative fashion can be accomplished through the use of appropriate techniques, such as transient elastography based on ultrasound (8), and Magnetic Resonance Elastography (MRE) based on magnetic resonance imaging (9).

In MRE, cyclic tissue displacements caused by shear waves induced in the tissue by an external actuator are quantified using phase-contrast imaging techniques. Through appropriate inversion algorithms the stiffness values can be reconstructed from the displacement values (10,11). MRE is in clinical use for assessing the progression of hepatic fibrosis (1) and has been applied for different purposes in other organs, such as the brain, spleen, kidney, pancreas, breast, heart, and skeletal muscles (12–14).

Current abdominal MRE acquisition requires patients to undergo multiple breathhold cycles, during which the breath is held for 10 - 20 seconds after exhalation (7). This limits the resolution and FOV due to short acquisition frames. Furthermore, it negatively impacts the patients overall experience of the exam and can pose significant issues or make an exam impossible for patient groups facing difficulties achieving the required breathhold durations, such as patients with pulmonary deficiencies, children and elderly (2). Insufficient breathhold durations cause motion artifacts as the patient starts breathing during acquisition, extending necessary scan time and possibly requiring the patient to be reexamined.

The objective of the work conducted is to identify and compare possible methods for reconstruction of free-breathing MRE data. Similar challenges requiring reconstruction of motion-binned MRI datasets are encountered in 4D-Flow and DCE imaging (15,16). Due to the similarity of these problems, appropriate methods for such sequences can be adapted to suit elastography data. Multiple reconstruction algorithms were adapted and applied to MRE data: zero-filling (ZF), interpolation, compressed sensing approaches based on a non-linear conjugate gradient descent (CG) and an iterative soft-thresholding method (IST) for determining minimal solutions to the image equation. The results are compared in regard to selected quality metrics and conclusions are drawn to allow the identification of appropriate reconstruction parameters and conditions under which they hold. To this means an evaluation framework has been implemented, allowing selection of the algorithm and corresponding parameters for fast evaluation using parameter lists.

In this work, a general overview to the utilized MRE acquisition scheme is given, as well as explanations of the evaluated algorithms and reconstruction parameters. Further, descriptions of the evaluation procedure and the utilized metrics for comparison of results are detailed. The results of the conducted experiments are presented and relevant findings are discussed.

Theory

Magnetic Resonance Elastography

The basic principle behind MRE is the measurement of displacements of individual voxels within the imaging volume under external mechanical excitation (17). Excitation can be performed by a variety of mechanical drivers, including, but not limited to electromechanical actuators, compressible chambers driven by pressure variation and mechanical vibrators (12,13). The main distinction between these actuators for experimental setup and patient experience is whether the source of the driving mechanical force is placed inside the bore in proximity to the place of actuation or externally whereby the pulses are transmitted by mechanical means to the patient. This excitation of well-defined single or multiple frequencies (18) provokes the propagation of shear waves within the tissues under examination. The cyclic displacements of the spins due to the occurring waves are then phase-encoded by synchronously switching bipolar motion encoding gradients (MEG), allowing an accumulation of phase shift. The total phase shift φ acquired during n wave cycles of a harmonic gradient waveform $\boldsymbol{G}$ of period τ_g can be expressed as (9):

$$\varphi(\boldsymbol{r},\theta) = \gamma \int_0^{n\tau_g<TE} \boldsymbol{G}(t)\cdot\boldsymbol{u}\cos(\boldsymbol{k}\cdot\boldsymbol{r} - 2\pi f_v t + \theta)\,dt \qquad [1]$$

where γ is the gyromagnetic ratio, $\boldsymbol{u}$ is the displacement magnitude of the spins around it's mean at position $\boldsymbol{r}$, and $\boldsymbol{k}$ is the wave vector of the mechanical excitation of frequency f_v and phase offset θ. MRE was first implemented with full-wave encoding, where one bipolar gradient cycle corresponded exactly to the vibration period, i.e. $\tau_g = \tau_v$, giving a lower limit for the minimal repetition times TR which can be used. In current GRE-based approaches fractional encoding (19) is commonly used, in which shorter gradient periods can be chosen, such that the encoding fraction $q = \frac{\tau_g}{\tau_v} < 1$. For fractional encoding methods the accumulated phase over a single gradient cycle ($n = 1$) is given by:

$$\varphi = \frac{\gamma\tau_g \boldsymbol{G}\cdot\boldsymbol{u}}{\pi}\cdot\frac{sin(\pi q)}{1-q^2} \qquad [2]$$

The motion sensitization and readout are implemented in an appropriate spin echo (SE) or gradient echo (GRE) sequence. Measurements are repeated with varying encoding directions according to a chosen MEG encoding scheme, such as 2-,4-, 6-point or Hadamard encoding and for several wave offsets θ. Various readout and acquisition strategies have been applied to MRE acquisition (20), that allow to reconstruct undersampled k-space data by exploiting underlying physical redundancies in the data, e.g. SENSE (21) or Compressed Sensing (22).

After acquisition, the data is sorted and arranged into a matching multidimensional array. Other than the spatial frequency dimensions $[k_x, k_y, k_z]$ as sampled in Fourier space, the data is also indexed along encoding directions $[d_{enc}]$, wave phases $[d_\theta]$ and respiratory states $[d_{res}]$. With the utilized acquisition scheme, there are 4 encoding directions, each spatial direction and a reference without motion encoding, 8 wave phase states separated by offsets in increments of $45°$, and an adjustable number of respiratory states as can be defined in respiratory motion-binning post acquisition. Due to the use of parallel imaging using information from several coils for data acquisition, the data also contains a dimension determining which coil acquired the given data $[d_{coil}]$.

Zero-filling and Interpolation

A reconstruction is performed to obtain an image from undersampled k-space data. Zero-filling reconstruction is implemented by setting empty entries of the data matrix to zero and applying the inverse Fourier transform along each of the directions $[k_x, k_y, k_z]$ to obtain a representation in image space $[x, y, z]$. Instead of filling the missing k-space entries with null values, they can be reconstructed from neighboring values through interpolation and/or extrapolation (23). This works best if the data is localized along the interpolation directions, i.e. the data must be sufficiently similar to its neighboring values. To this means two interpolation variants have been implemented. In both cases the data is rearranged in a 2-dimensional array, whereby the order in which this reshaping is performed must be chosen so as to represent the proximity of the data along each of its dimensions. In the first implementation, the data is interpolated along two concatenated dimensions of the reshaped array, in our case along the mechanical wave phase dimension $[d_\theta]$ and the encoding direction $[d_{\mathrm{enc}}]$. A representation of the reshaped data matrix is displayed in Figure 1a. This method is subsequently referred to as *1D-Interpolation*. Similarly, in the second implementation the data is rearranged and the resulting 2-dimensional array is interpolated along both directions with a chosen 2-dimensional interpolation method, referred to as *2D-Interpolation*. Allowing proximity along more than one data dimension, in our case the wave phases $[d_\theta]$ and the fully sampled spatial dimension $[x]$, to be leveraged. The data matrix arrangement used in this method is shown in Figure 1b. Interpolation is performed for each coil element separately and a final result is combined through coil combination.

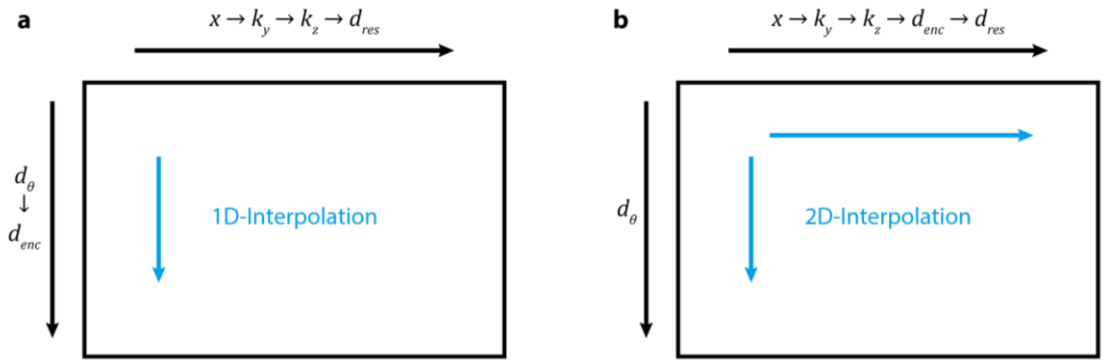

Figure 1: Depiction of the reshaped data matrices as used for (a) 1D-Interpolation and (b) 2D-Interpolation

Compressed Sensing

Specialized methods for handling low k-space sampling rates have been developed in the past decade. Image reconstruction techniques exploiting the inherent sparsity of natural images under certain transforms allow reconstructing important features from relatively few data points (22,24). Such Compressed Sensing (CS) methods have found wide acceptance for image reconstruction in a broad range of MRI applications (25–27). The actual reconstruction is given by finding minimal solutions to the optimization problem:

$$\boldsymbol{x} = \min_{x} \|\boldsymbol{F} \cdot \boldsymbol{C} \cdot \boldsymbol{x} - \boldsymbol{y}\|_2^2 + \lambda_{S1} \|\boldsymbol{S}_1 \cdot \boldsymbol{x}\|_1 + \lambda_{S2} \|\boldsymbol{S}_2 \cdot \boldsymbol{x}\|_1 \qquad [3]$$

where $\boldsymbol{y}$ is the multicoil k-space data, $\boldsymbol{F}$ the sampling Fourier transform, $\boldsymbol{C}$ the coil sensitivity matrix, and $\boldsymbol{S}_1, \boldsymbol{S}_2$ are transformations of the signal into sparse domains with regularization weights λ_1, λ_2. The data consistency term uses the Euclidian ℓ_2-norm, whereby the ℓ_1-norm terms promote sparsity. Two algorithms to find minimal solutions of [3] were adapted for MRE from similar image

reconstruction problems: a *non-linear conjugate gradient* method based on the idea of regularization along multiple dimensions as in XD-GRASP (3,22) and an *iterative soft-thresholding* approach implementing Low-rank plus Sparse reconstruction (4). The first algorithm relies on a backtracking line search $(\alpha = 0.01; \beta = 0.6)$ performed during each iteration of the gradient method. The second algorithm additionally separates the solution into sparse and low-rank components $(\boldsymbol{x} = \boldsymbol{x}_S + \boldsymbol{x}_L)$, and adds a further matrix-norm term $\lambda_L \|x_L\|_*$ to the optimization problem [3] to enforce low-rankness of the solution part, where the sparsifying transforms are only applied to $\boldsymbol{x}_S$. For reconstruction of the low-rank and sparse components the data is rearranged into a Casorati matrix by concatenating the spatial dimensions $[k_y\,, k_z]$ and the additional MRE dimensions $[d_\theta\,, d_{res}]$. In both methods the reconstruction is performed by iterating over the remaining dimensions $[x\,, d_{enc}]$.

The application of compressed sensing to MRI necessitates an incoherent sampling scheme and a sparse representation in a chosen transform domain (24). Incoherence is fulfilled by designing an appropriate sampling pattern. To optimally fulfill the second criterium, several sparsifying transforms were analyzed in the scope of this work to determine the suitability for application to MRE reconstruction. A commonly used transform to sparsify natural images is total variation (TV), i.e. the sum of the finite-differences along a chosen dimension or several chosen dimensions. Furthermore, considering the sinusoidal nature of mechanical waves for excitation of the tissue, the Fourier transform along the wave phase $[d_\theta]$ was implemented to verify its utility for use as a sparsifying transform for MRE. Other transforms that were implemented are the wavelet transform and the discrete cosine transform (DCT), in popular use in the compression algorithm behind the JPEG file format (28). The sparsifying transforms principally differ according to which dimensions they act on and can be grouped into spatial transformations which act on each image slice in two of the three spatial dimensions separately $[k_x\,, k_y\,, k_z]$ and extra-dimensional transformations acting along one of the additional dimensions $[d_{enc}\,, d_\theta\,, d_{res}]$.

Methods

Data Acquisition

For the verification of the implemented reconstruction algorithms MRE data was gathered on a gel phantom with four circular inclusions of varying stiffness (CIRS Inc., Norfolk, VA). The measurements were performed using a GRE-based fractional MRE sequence with repetition time $TR = 10\,ms$ and $20°$ flip angle on a 3T Philips Ingenia MR system (Philips Healthcare, Best, the Netherlands), whereby the signal was received by a 15-channel head coil array. A TTL-triggered electro-mechanical actuator was used to induce shear waves of frequency $f_v = 100Hz$ in the phantom and $12\,\frac{mT}{m}$ bipolar MEGs at a frequency $f_g = 180\,Hz$ $(q = 0.56)$ were applied at 8 different phase offsets in $45°$ steps. Data was acquired separately with motion-sensitization applied in all three spatial dimensions and a reference without encoding to obtain the full displacement vector field.

A Cartesian readout was used to acquire a 112×112 imaging matrix for 14 slices with isotropic resolution of $2\,mm$ and slice gap of $0.2\,mm$. The resulting full volumetric dataset was reconstructed and used as the ground truth for all subsequent experiments and evaluation. From the complex raw values the displacements were calculated and the stiffness values were reconstructed by an MRE inversion algorithm (29).

Simulation

To evaluate the reconstruction algorithms and determine optimal acquisition parameters a typical MRE acquisition was performed in-silico on the ground truth dataset. The simulation consisted of three parts, completed in order:

1. **Respiratory movement simulation**

   To verify the feasibility and quality of our reconstruction methods applied to a free-breathing MRE acquisition, respiratory movement was simulated by sorting the ground truth data into a variable number of respiratory states along an additional data dimension $[d_{res}]$, as would be performed during motion-binning using data obtained by a method for tracking respiration in-vivo, such as external trackers or MR navigators (15). Each motion bin was filled with a copy of the original data and each state other than the exhaled ground state was shifted by a slight amount along the fully sampled frequency encoding dimension $[x]$. For reconstruction evaluation 4 states with a shift of $4\ mm$ between states were simulated, the results of which can be seen in Figure 2.

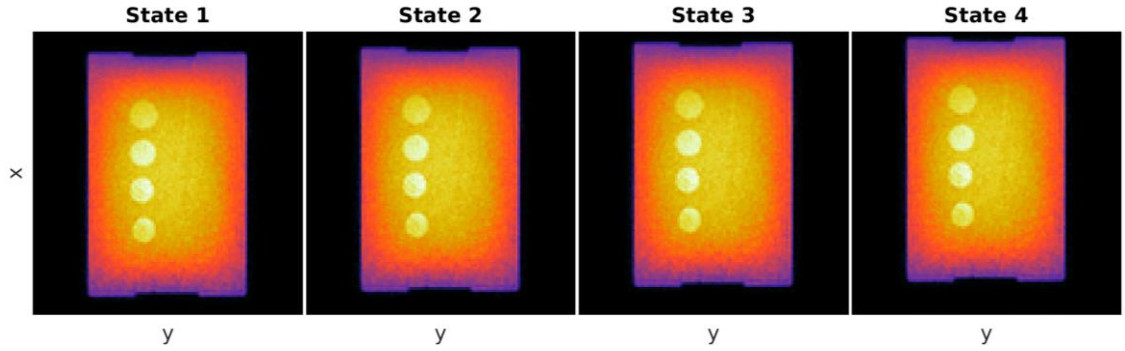

Figure 2: The same $[x, y]$ slice viewed in each of the simulated respiratory states moving along $[x]$.

2. **Parallel acquisition (SENSE) simulation**

   Simultaneous acquisition by several receiver coil elements was mimicked by adding an additional coil dimension $[d_{coil}]$ to the dataset. Each entry along the new dimension was filled by applying a coil sensitivity map to a copy of the ground truth data. The number of coil elements was determined by a separate simulation parameter. The maps could be either calculated from a geometrical model, as seen in Figure 3, or measured coil sensitivities from the phantom acquisition could be used.

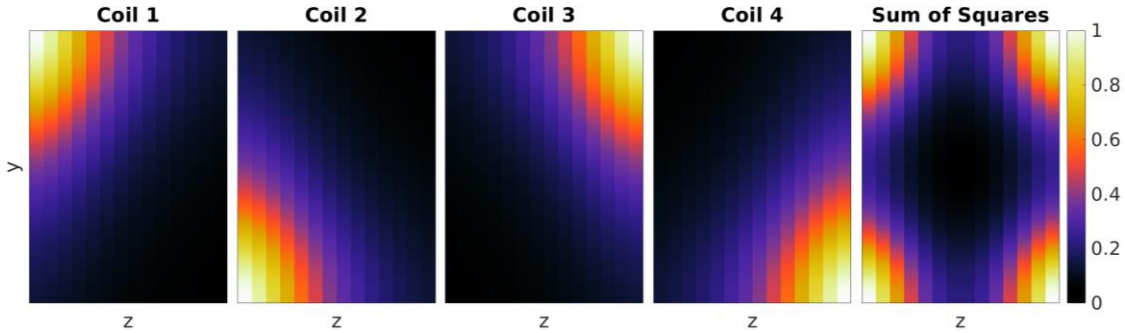

Figure 3: Coil sensitivity maps as calculated from the geometric model. The sensitivities are constant along the displayed cross-sections along $[x]$. On the far right the sum of squares of all sensitivity maps combined as used for scaling during coil combination. i.e. Roemer Reconstruction (30).

3. Sampling simulation

A pseudo-radial Cartesian sampling pattern based on golden-angle acquisition schemes (26) was used in our simulation. A simulation parameter determined the number of sampling points in the $[k_y, k_z]$ plane, whereby the $[k_x]$ dimension was fully sampled. The pattern consists of lobes around radial extensions from the k-space center, each containing 31 consecutive sample points extending and then returning to the center. A depiction of the pattern is displayed in Figure 4. Each consecutive point was attributed to a different element in the $[d_{enc}, d_\theta]$ plane, hence establishing a high degree of incoherence needed for CS reconstruction and ensuring that for each of the encoding directions and mechanical wave phases the k-space center is sampled several times. This data can potentially be used for respiratory navigation or self-gating (31,32) without the need for acquiring additional navigator slices. Repeated sampling points were ignored since they cannot provide additional information in the simulation, whereas in an actual acquisition the samples could be averaged to increase SNR.

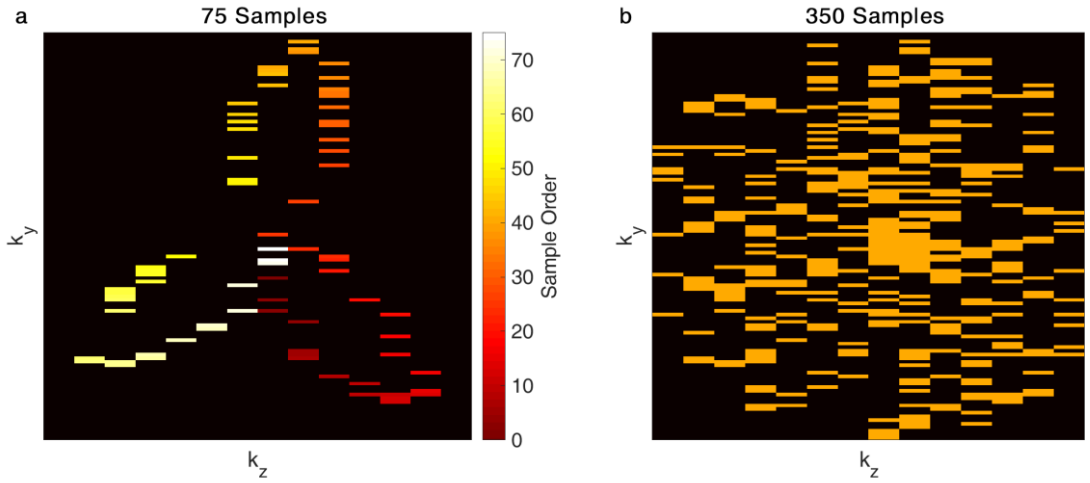

Figure 4: Sampling pattern used for simulation of an undersampled acquisition on the 112×14 *imaging matrix along the* $[k_y, k_z]$ *dimensions for (a) 75 sampling points and (b) for 350 points. Note the radial lobes consisting of 31 sample points and separated by the golden angle* $\varphi_g \approx 137.51°$.

Evaluation

An evaluation framework was implemented in MATLAB (Mathworks, Natick, Massachusetts, USA) to compare the performance of the five reconstruction algorithms. Simulation parameters and an array of reconstruction parameters were read from an input file, the simulation was carried out accordingly and reconstruction performed for each parameter set. Quality metrics were calculated and the results stored. First the respiratory motion simulation was left out to determine parameters settings yielding satisfactory reconstruction results. Next, reconstruction was tested on motion-binned data and compared to results without respiratory states at similar sampling rates. Finally, minimal sampling rates satisfying chosen objectives were determined.

All parameters were read from structured text files, allowing batch reconstruction jobs to be defined and executed. An overview of the reconstruction parameters for each algorithm and sparsifying transformation is given in Table 1.

a	Reconstruction algorithm	Parameter	Description (Typical Values)
	Zero-filling	None	
	1D-Interpolation	Interpolation type	(nearest neighbor, linear, cubic, spline)
		Extrapolation	Same as interpolation type (Boolean)
		Order	Matrix permutation order ($[1,2,3,6,4,5]$)
	2D-Interpolation	Interpolation type	(nearest neighbor, linear, cubic, natural neigh.)
		Extrapolation type	(nearest neighbor, linear)
		Order	Matrix permutation order ($[1,2,3,4,6,5]$)
	Conjugate Gradient	Gradient tolerance	Convergence stopping criteria (10^{-4})
		Iteration limit	Stopping criteria $(200 - 1000)$
		Transforms S_1 / S_2	See below (b)
	Iterative Soft-Thresholding	Step tolerance	Convergence stopping criteria $(10^{-6} - 10^{-15})$
		Iteration limit	Stopping criteria $(600 - 2500)$
		Low-rank threshold	λ_L $(10^{-1} - 10^{-4})$
		Transforms S_1 / S_2	See below (b)

b	Sparsifying Transform	Parameter	Description (Typical Values)
	Identity	Penalty	λ_S $(10^{-3} - 10^{-6})$
	Spatial Total Variation	Penalty	λ_S $(10^{-3} - 10^{-6})$
	Discrete Cosine Transform	Penalty	λ_S $(10^{-3} - 10^{-6})$
		Block Size	Coarsity of transform
		Overlap	Overlap between blocks
	Discrete Wavelet Transform	Penalty	λ_S $(10^{-3} - 10^{-6})$
		Wavelet Type	(Haar, Beylkin, Coiflet, Daubechies, Symmlet, Battle, Vaidyanathan)
		Length	Number of samples of the wavelet $(2 - 15)$
		Scale	Recursion depth $\left[\log_2 L_y - 1, \log_2 L_z - 1\right]$
	Fourier Transform	Penalty	λ_S $(10^{-3} - 10^{-6})$
		Dimension	Transform along given dimension $(3 \rightarrow d_\theta)$
	Total Variation	Penalty	λ_S $(10^{-3} - 10^{-5})$
		Dimension	Transform along given dimension $(4 \rightarrow d_{res})$

Table 1: Overview of reconstruction parameters for each (a) algorithm and (b) sparsifying transform.

Various root mean square errors (RMSE) were calculated against the ground truth for each step in the stiffness reconstruction: absolute magnitude, phase, displacement magnitude, displacement phase, loss modulus, shear modulus and Young's modulus. The RMSE values were calculated according to the following equation, where x is one of the aforementioned values of the reconstruction and x_{GT} the corresponding ground truth value, for each of the N values of the region of interest:

$$RMSE = \frac{1}{\sqrt{N}} \sqrt{\sum (x_{GT} - x)^2} \qquad [4]$$

Moreover, the displacement-to-noise ratio (DNR) was calculated for each reconstructed dataset. DNR is an important metric in elastography, indicating the noise level and allowing an assessment of regularization used in compressed sensing approaches. DNR is calculated by averaging the ratio of the displacement signal s_u and the standard deviation of the noise σ_η for all N observed samples:

$$DNR = \frac{1}{N}\sum \frac{s_u}{\sigma_\eta} = \frac{1}{N}\sum \frac{2 \cdot U_1}{\sqrt{\frac{1}{N-1}\Sigma(\eta - \bar{\eta})^2}} \quad [5]$$

Here U_0 designates the constant term (DC-component) and U_1 the first non-constant term of the discrete Fourier transform of the displacement field along the mechanical wave phases $[d_\omega]$. Since the displacements are sinusoidal in the ideal case, the noise η in the displacement field is given by the unwanted signal in the harmonics of the Fourier transform $\eta = U - U_0 - 2 \cdot U_1$, where $\bar{\eta}$ is the average noise level.

The final metric used in assessing reconstruction quality is the displacement correlation. A linear model without intercept was fitted to the reconstructed displacement values u correlated to the corresponding ground truth value u_{GT} . The slope m, as well as the average spread σ_u of the correlated values from the ideal, given by the RMS error against the perfectly correlated model, are valuable determinants of quality.

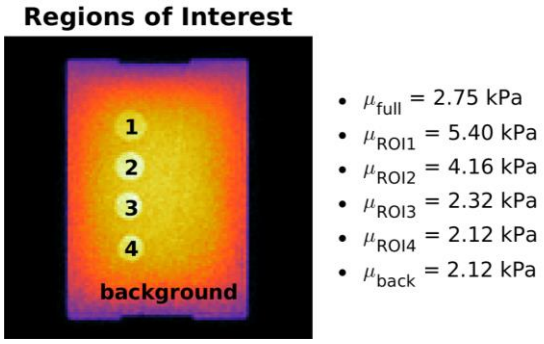

Figure 5: Each of the metrics can be calculated for different regions of interest (ROI). Geometrical ROIs in the phantom were defined, one for each of the inclusions of differing stiffness (inclusion $1-4$, from least stiff to stiffest), the background and the entire region of the phantom. In this way observations and comparisons of reconstruction effects on regions of varying size and stiffness could be made.

Results

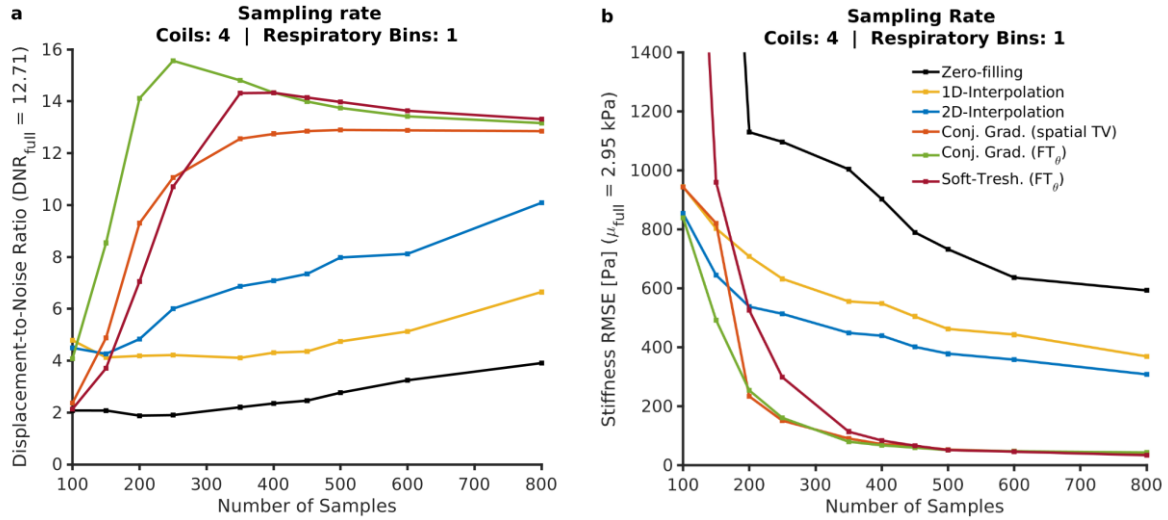

Figure 6: Comparison of all implemented reconstruction algorithms for varying sampling rates (from approx. $5.8\% - 36.9\%$ of all k-space samples). The zero-filling and interpolation approaches yield several times larger RMS errors compared to the algorithms utilizing CS. Higher sampling rates offer better results for all algorithms, however, shorter acquisition is desirable.

Using the implemented framework, parameters were varied to determine values yielding satisfactory results measured by the established quality metrics. To estimate optimal parameters for elasticity reconstruction no respiratory motion was simulated. Once the effect of the different parameters was understood, the reconstruction was implemented on datasets including simulated respiratory motion. Firstly, the algorithms were compared against each other for varying sampling rates, as displayed in Figure 6. The compressed sensing methods provided higher DNR and lower RMSE values across all intermediate reconstruction steps (magnitude, phase, displacement), and the stiffness results compared to zero-filling and interpolation algorithms for lower sampling rates. The zero-filling / interpolation approach was not investigated further, whereas a sampling rate of $\sim 19.0\%$ (350 samples or a fivefold undersampling) was deemed adequate to further investigate both CS implementations. The algorithms iteratively approximate minimal solutions to the optimization problem [6], hence stopping criteria need to be defined to trade-off reconstruction time and quality. Figure 7 shows the effect of varying the maximum number of iterations if no further stopping criteria are used to determine convergence.

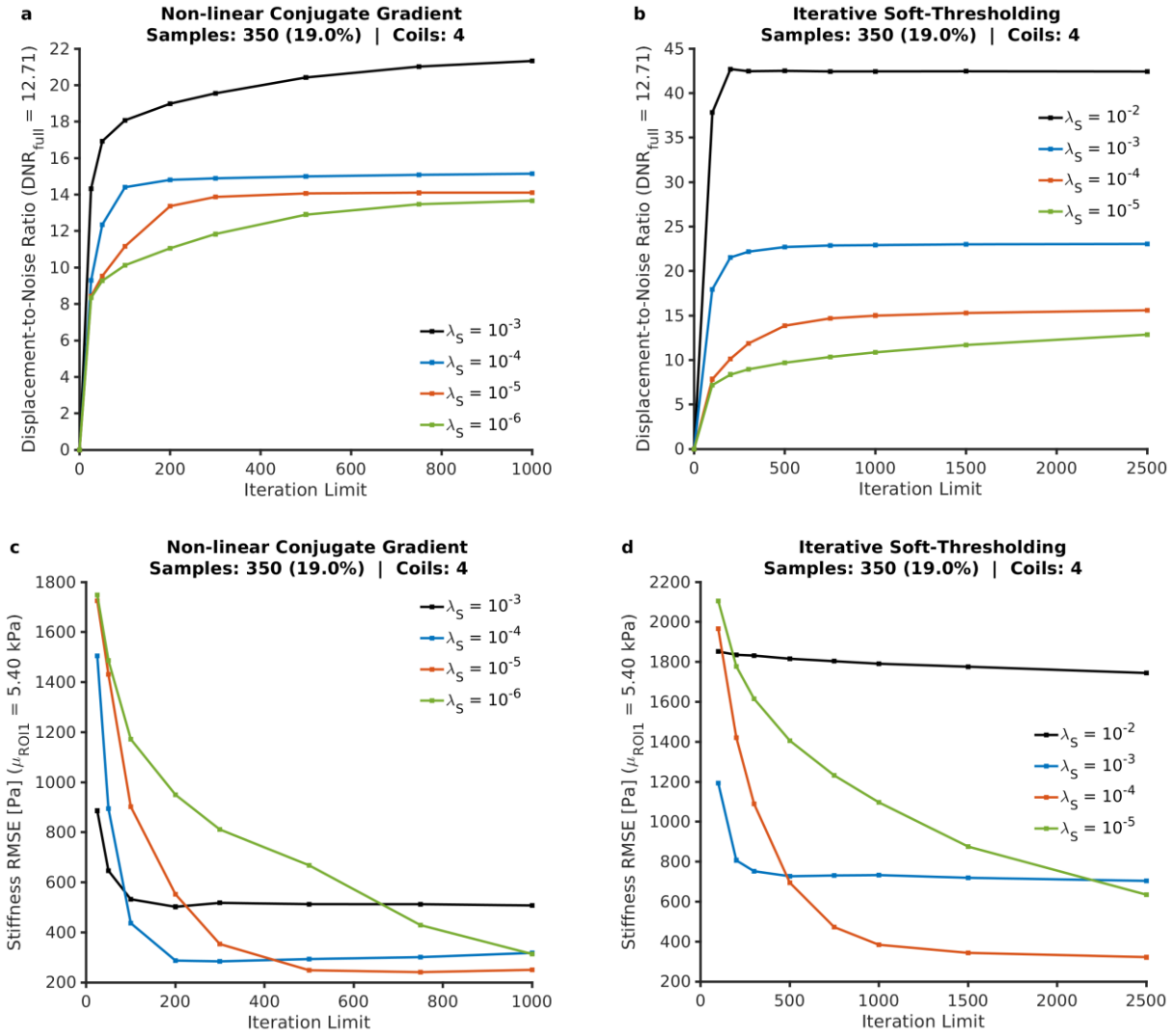

Figure 7: Effect of increasing the number of iterations on reconstruction outcome. In all cases the Fourier transform in d_θ was used for regularization during iterative reconstruction. DNR can attain values above ground truth for stronger regularization (a-b). Reconstruction with more heavily weighted regularization requires more iterations to converge, but converges with smaller deviations from the ground truth (c-d).

Compressed sensing relies on the ability to represent the signal with a high degree of sparsity in a suitable transform domain (22). To accurately reconstruct mechanical properties from MRE data suitable transformations need to be implemented capable of providing sparse representations of the data including not only spatial information, but also additional encoding and motion dimensions. One of our initial postulates was that the mechanical wave phase has a theoretically ideally sparse representation in the Fourier domain given its sinusoidal nature. Using this for regularization it is possible to suppress noise in the reconstructed signal and hence achieve high DNR as observed in Figure 7a and Figure 7b. Further sparsifying transforms adapted for MRE from prior work (4,24) are compared and results are displayed for varying weights / thresholds in Figure 8 below. Multiple sparsifying transforms can be utilized in parallel with different weighting, allowing distinct regularization along other data dimensions, such as the respiratory motion in navigated MRE acquisition. Here, the focus was set on finding good parameters for reconstruction of the desired mechanical properties in a first step, and hence a single sparsifying transform was tested on data without respiratory bins.

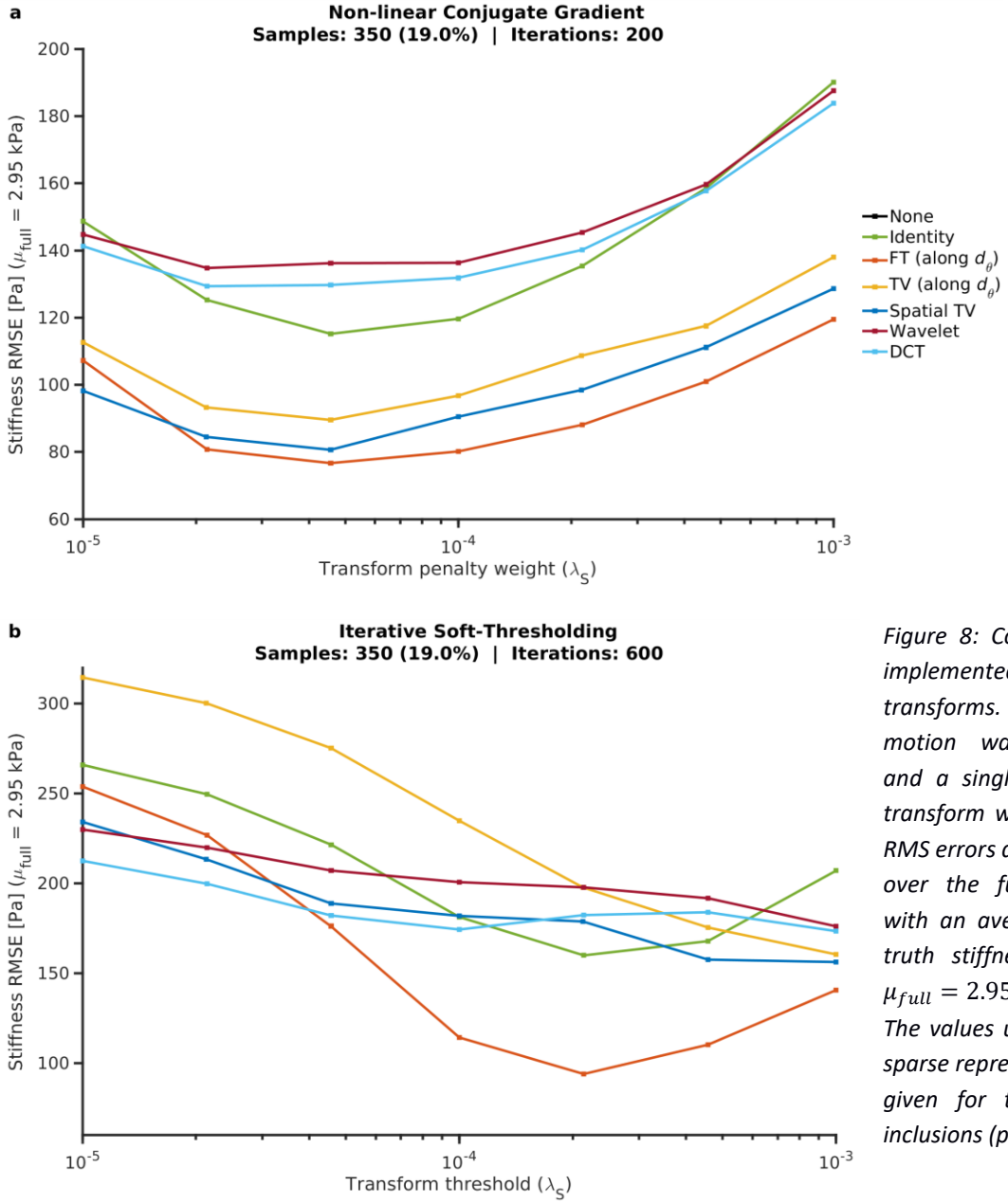

Figure 8: Comparison of implemented sparsifying transforms. No breathing motion was simulated and a single sparsifying transform was used. The RMS errors are calculated over the full phantom, with an average ground truth stiffness value of $\mu_{full} = 2.95\ kPa$ *(a-b). The values using* FT_θ *for sparse representation are given for the separate inclusions (p.12 c-d).*

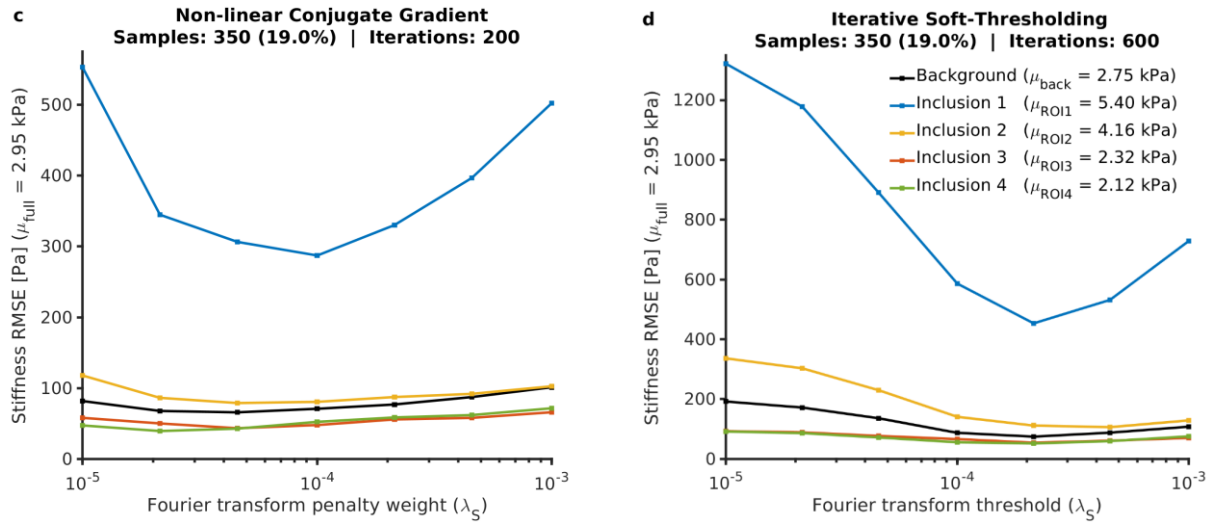

There is a tendency for large values to be underestimated, as can be seen in Figure 8c and Figure 8d where there is a comparatively large absolute error for the stiffest inclusion, resulting in a larger relative error. Since displacement amplitude in the sample is inversely proportional to the stiffness, the largest displacements can be observed in the fourth inclusion which has the lowest stiffness. The same underestimation effect can be seen for the large displacements in this inclusion (additional figures comparing different quality metrics can be found in the appendix).

Based on the comparisons made above, further evaluation focused on the use of the wave phase Fourier transform FT_θ as the sparse representation for both CS approaches. Regularization weighting has an observable impact on reconstruction quality in all chosen metrics. Furthermore, the utilized soft-thresholding optimization allows the inclusion of low-rank regularization in addition to the data consistency and sparse terms. Estimating the effect of the various weightings on the outcome can be challenging, hence an extensive evaluation was performed for each parameter.

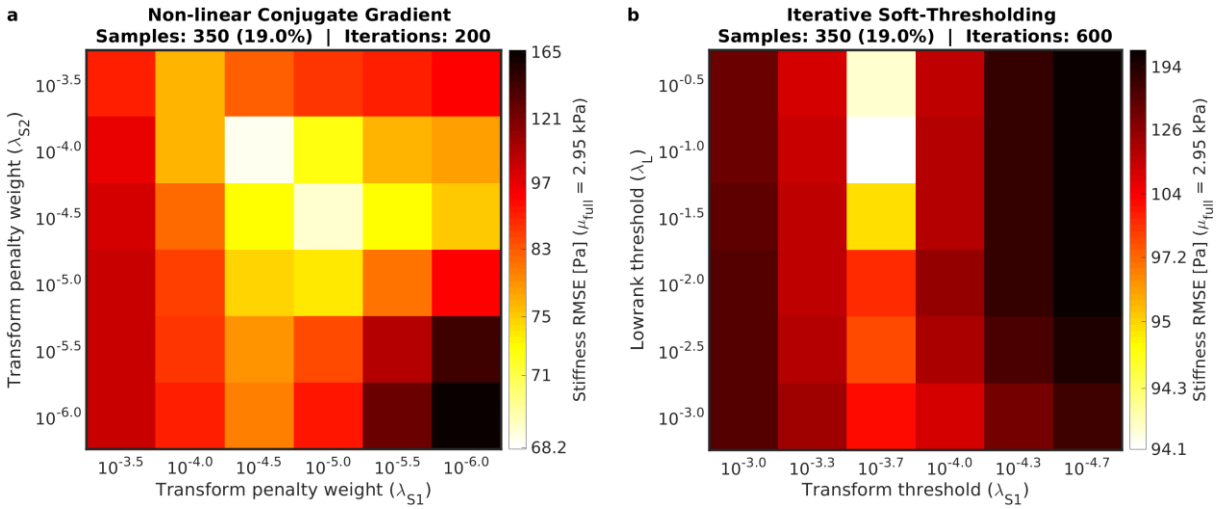

Figure 9: Effects of varying regularization weighting for the conjugate gradient algorithm using FT_θ and spatial TV as sparse signal representations (a), and for the soft-thresholding algorithm implementing a low-rank regularization and FT_θ sparse regularization (b). Further figures comparing different quality metrics for the same parameters can be found in the appendix.

The observed minima in RMS errors in all steps of the processing suggest that a balance must be struck between data-consistency and minimizing the chosen ℓ_1 norm enforcing transform sparsity or ℓ_* norm enforcing low-rankness. To prevent over-/ underfitting the reconstruction to the acquired undersampled data appropriate regularization weighting for the problem must be chosen. For the MRE reconstruction using FT_θ as a sparsifying transformation, the over-/underfitting manifests primarily in an underestimation of high stiffness values, as well as visible coarsity in the case of overfitting or regular streaking in the case of underfitting to the sampled data, shown in Figure 10.

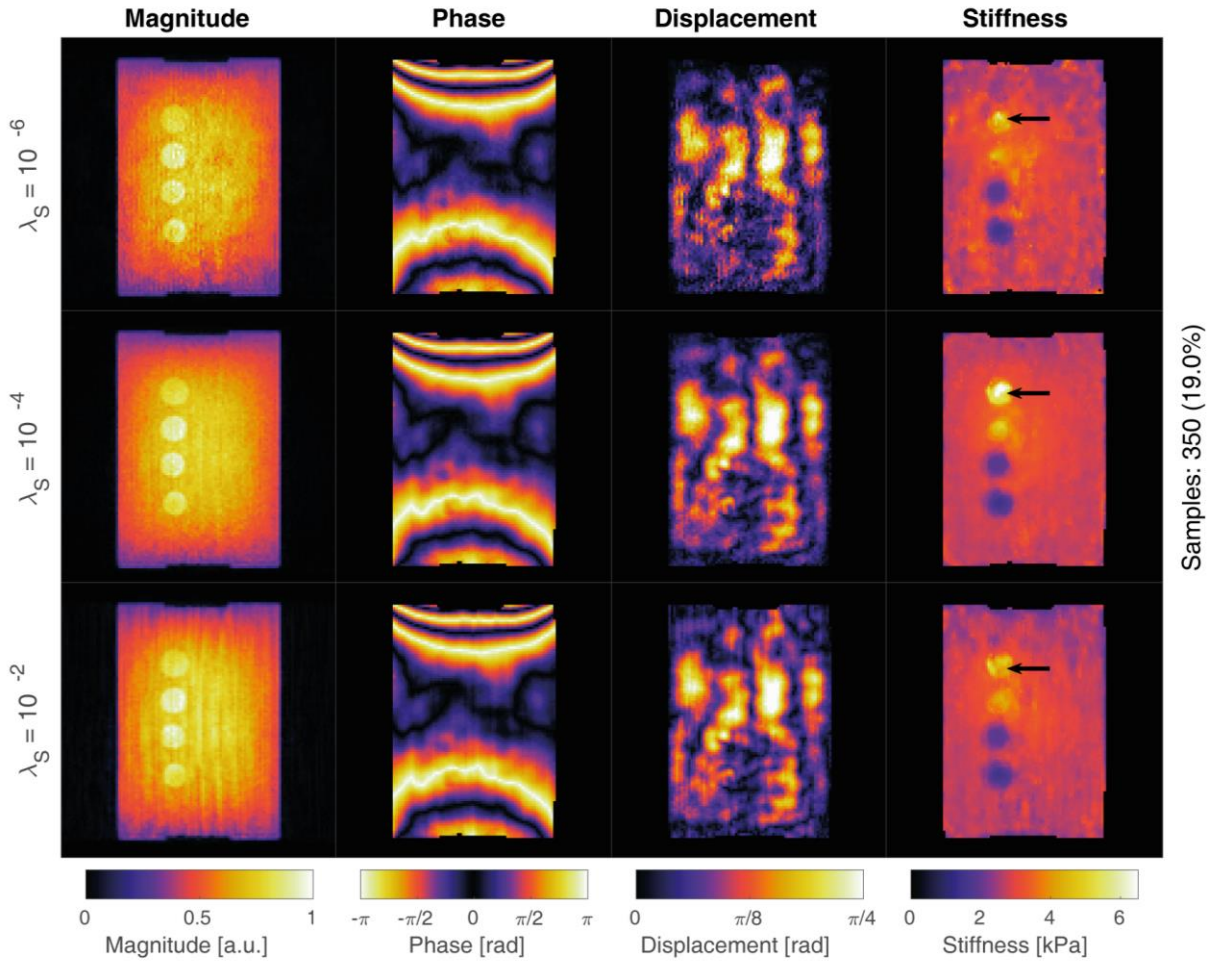

Figure 10: Examples of too little (top), suitable (middle) and too strong regularization (bottom) obtained after 600 iterations of the soft-thresholding algorithm with low-rank weighting of $\lambda_L = 10^{-1}$ and varying weights for the sparse term using FT_θ The magnitude images clearly exhibit a coarse noisy appearance when overfitting to the sampled data ($\lambda_S = 10^{-6}$) and streaking when the data consistency term is less weighted compared to the regularization term ($\lambda_S = 10^{-2}$). Both cases cause an underestimation of stiffness in the stiffest inclusion and less homogeneous values in the phantom background.

Respiratory Motion Regularization

Respiratory motion was simulated on the phantom where samples were binned sequentially to one of the four states. The first state was chosen as the exhaled state and 40% of the samples were assigned to this state. The remaining three states were each filled with 20% of the full number of samples. For evaluation, a total of 875 samples were chosen, corresponding to the same sampling density in the ground state used for prior evaluation without respiratory simulation ($875 \cdot 0.4 = 350$). The

regularization weighting was optimized for both methods (Figure 11) and the best results were selected for further comparison. The results after respiratory motion simulation were compared in the ground motion state, since the sampling density in this state is equal to the density without motion simulation (Figure 12).

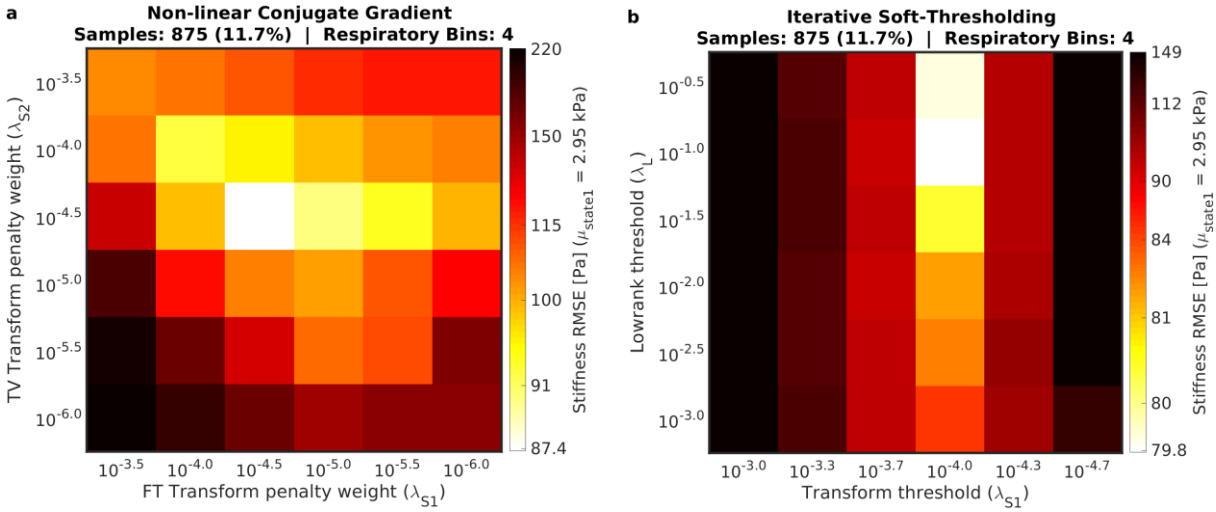

Figure 11: Effects on reconstructed respiratory ground state stiffness RMSE with varying regularization weighting. (a) Conjugate gradient algorithm using two sparsifying transforms: the Fourier transform along the mechanical wave phase ($S1$) and total variation along the respiratory phase ($S2$) limited to 500 iterations. (b) Results for the soft-thresholding algorithm using low-rank and FT_θ regularization with an iteration limit of 1250. Further figures comparing different quality metrics for the same parameters can be found in the appendix.

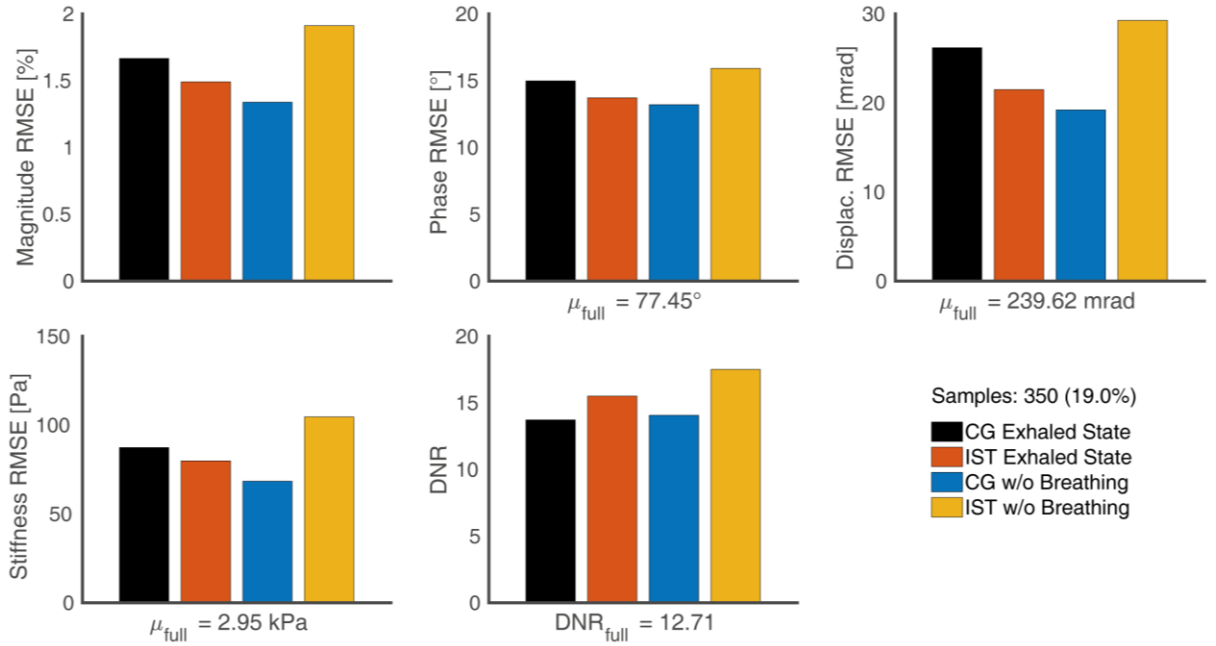

Figure 12: Comparison of both compressed sensing implementations using a non-linear conjugate gradient method (CG) or iterative soft-thresholding (IST) for reconstruction of the exhaled state. Parameter optimization was performed previously (s. Figure 9 and Figure 10). For motion simulation, the sampling rate in the exhaled state was equal to the rate when no respiration was simulated (350 samples or 19.0% of full k-space), whereas the other respiratory states had a lower sampling rate (175 samples or 9.5% of k-space).

Discussion

Common approaches to respiratory motion correction in MRI include gating the acquisition to the motion state, or eliminating motion altogether with breathholds. The scan efficiency is hereby intrinsically lower, since a smaller fraction of total scan time is utilized for acquiring data that will be used in reconstruction. The proposed compressed sensing approach aims at exploiting correlation among motion states in reconstruction. This principle has been previously demonstrated for other imaging techniques such as dynamic contrast-enhanced MRI (3,27,33), but it remains to demonstrate utility for MR Elastography.

In principle, compressed sensing can efficiently exploit underlying correlations given that the data has a sparse representation in a known transform domain. We postulate that the acquired elastography data has a sparse representation given by the Fourier transform in the wave phase dimension (FT_θ) due to the sinusoidal nature of the phase offsets. We further expect a simultaneous TV regularization of motion states (TV_{res}) to aid in reconstruction of respiratory states besides the ground state, due to the relatively small differences between frames which we observe.

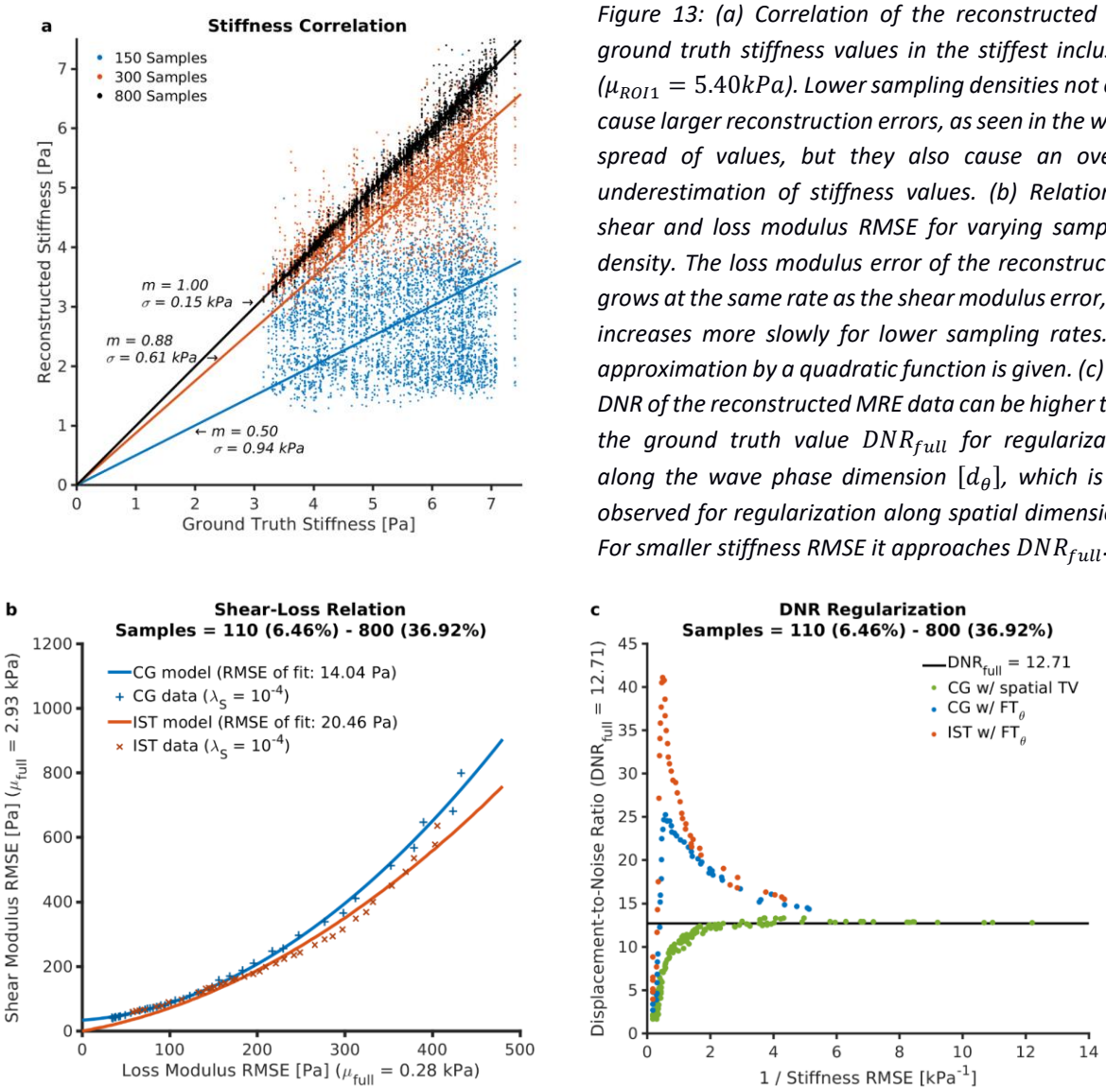

Figure 13: (a) Correlation of the reconstructed and ground truth stiffness values in the stiffest inclusion ($\mu_{ROI1} = 5.40kPa$). Lower sampling densities not only cause larger reconstruction errors, as seen in the wider spread of values, but they also cause an overall underestimation of stiffness values. (b) Relation of shear and loss modulus RMSE for varying sampling density. The loss modulus error of the reconstruction grows at the same rate as the shear modulus error, but increases more slowly for lower sampling rates. An approximation by a quadratic function is given. (c) The DNR of the reconstructed MRE data can be higher than the ground truth value DNR_{full} for regularization along the wave phase dimension $[d_\theta]$, which is not observed for regularization along spatial dimensions. For smaller stiffness RMSE it approaches DNR_{full}.

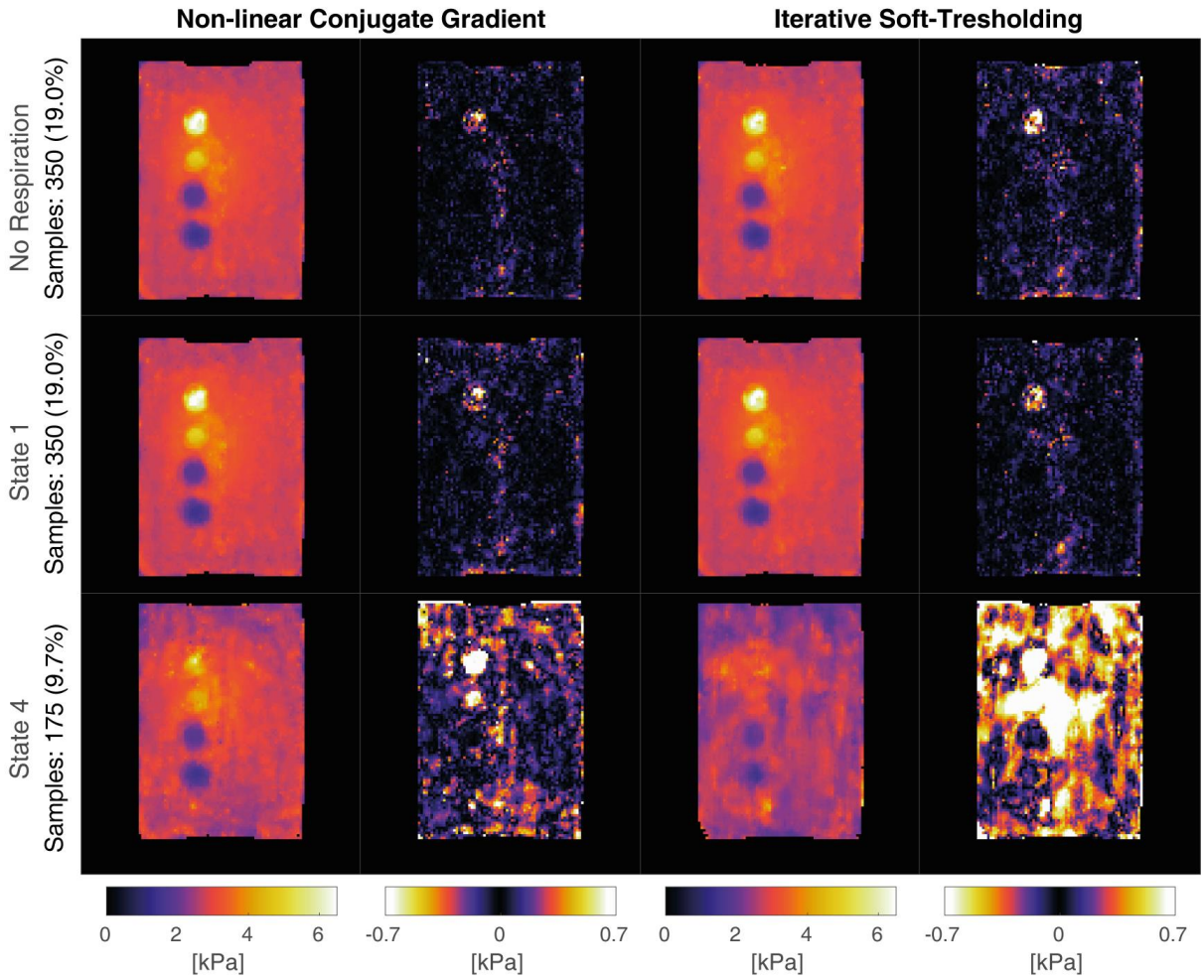

Figure 14: Reconstructed elastograms and the corresponding deviation from the ground truth: (top) without motion-simulation; (middle) ground state of four motion bins; (bottom) last state corresponding to the largest displacement, i.e. full inhalation. Both methods yield similar results without clearly visible differences in the ground state, which was more heavily sampled, as would be the case during exhalation in free-breathing acquisition. The conjugate gradient approach implements TV regularization along $[d_{res}]$ *and enables all four inclusions to be resolved even in state 4, albeit with a decreased overall image quality due to the lower sampling rate (*9.5% *of all* k*-space values).*

The results obtained confirm that FT_θ regularization provides the best reconstruction quality using both the conjugate gradient and the soft-thresholding algorithm (Figure 8). A major shortcoming of the proposed regularization is the underestimation of large values as seen in Figure 13a. However, interpretation is difficult and depends on the chosen quality metrics. DNR can provide insights into intermediate reconstruction results, but even poorly reconstructed elastograms can exhibit high DNR in case of strong regularization, hence the decisive metric of quality was the RMSE of the final elastograms. It should be noted that the quality of reconstruction of shear and loss components of stiffness scale differently (Figure 13b), hence a comprehensive analysis needs to compare multiple metrics.

The evaluation on data with motion simulation suggests that the TV_{res} regularization allows the reconstruction of higher motion states while preserving the reconstruction quality in the ground state (Figure 14). This contrasts with the results obtained by applying low-rank matrix completion to resolve the simulated motion where the ground state is reconstructed, but we observe no improvement in

higher states for the examined sampling rates (Figure 15). We assumed a simple motion model for simulation, modelling only translation as the most important component contributing to motion-blurring. A more realistic model encompassing compression and non-linear shifts, or *in vivo* acquisition, might prove more difficult to reconstruct using the suggested regularization. The clinical value of resolving different motion-states needs to be determined in future work, but improvements in patient comfort are likely to allow rapid acceptance if they do not come at the cost of increased scan times, or reduced resolution and accuracy.

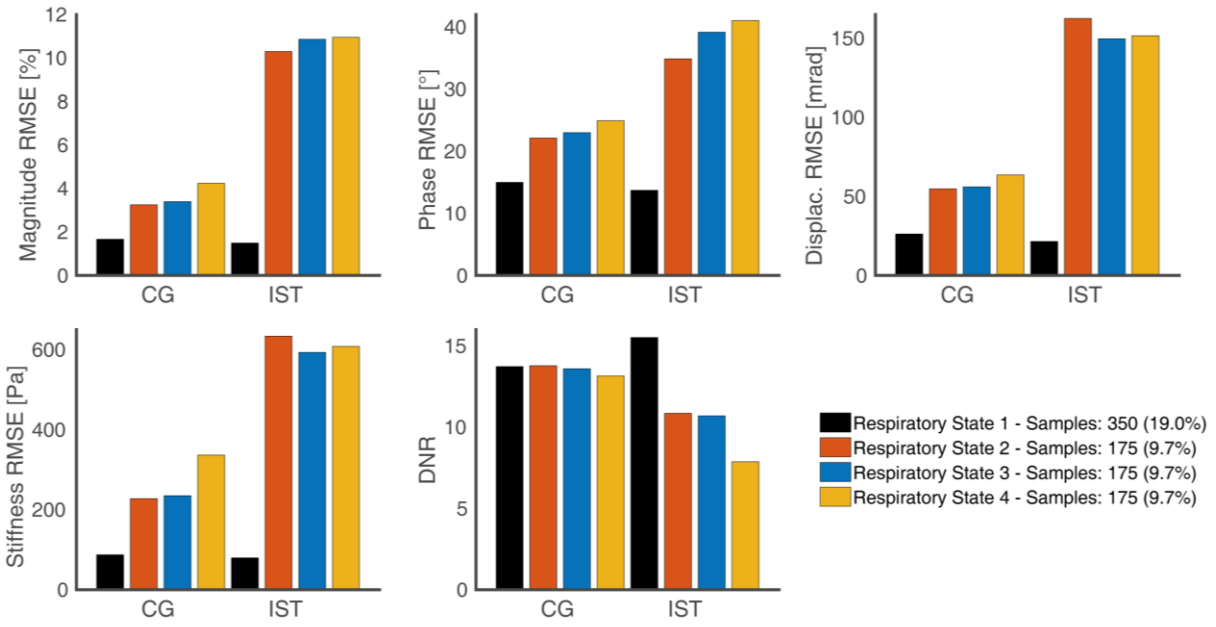

Figure 15: Side-by-side comparison of the motion-resolved conjugate gradient and soft-thresholding reconstruction algorithms for each respiratory state. Overall, the quality of reconstruction is highest in the lowest state, roughly equal in the intermediate states, and worse in the final state. Note that the algorithms achieve comparable results in the ground state, but the conjugate gradient method, implementing TV_{res} regularization, reconstructs higher states better than the soft-thresholding approach implementing low-rank regularization.

Conclusion

In this proof-of-concept study, we demonstrated compressed sensing reconstruction for respiratory motion-resolved MRE. A comparison of sparsifying transforms and regularization parameters was made. The results indicate that the Fourier transform along the mechanical wave phase is a suitable sparsifying transformation for MRE data. Findings suggest that the application of motion state TV regularization could potentially aid in the reconstruction of elastograms for all phases of the respiratory cycle in free-breathing MRE. We investigated the limits of acquisition parameters such as sampling density for prospective free-breathing elastography methods through simulated acquisitions with varying parameters.

Further work is needed to examine and optimize the application of the suggested reconstruction methods *in vivo*. The potential clinical impact of an accurate and sensitive implementation of free-breathing MRE is left to be shown in practice. However, increased patient comfort, and a better understanding of changing stiffness in abdominal organs under varying external pressure during the breath-cycle, are promising indicators for such a method to be adopted in clinical routine.

References

1. Singh S, Venkatesh SK, Wang Z, et al. Diagnostic performance of magnetic resonance elastography in staging liver fibrosis: A systematic review and meta-analysis of individual participant data. Clin. Gastroenterol. Hepatol. 2015;13:440–451. doi: 10.1016/j.cgh.2014.09.046.

2. Murphy IG, Graves MJ, Reid S, Patterson AJ, Patterson I, Priest AN, Lomas DJ. Comparison of breath-hold, respiratory navigated and free-breathing MR elastography of the liver. Magn. Reson. Imaging [Internet] 2017;37:46–50. doi: 10.1016/j.mri.2016.10.011.

3. Feng L, Axel L, Chandarana H, Block KT, Sodickson DK, Otazo R. XD-GRASP: Golden-angle radial MRI with reconstruction of extra motion-state dimensions using compressed sensing. Magn. Reson. Med. 2016;75:775–788. doi: 10.1002/mrm.25665.

4. Otazo R, Candès E, Sodickson DK. Low-rank plus sparse matrix decomposition for accelerated dynamic MRI with separation of background and dynamic components. Magn. Reson. Med. 2015;73:1125–1136. doi: 10.1002/mrm.25240.

5. Burke P, Eley R, Heyl S, McGuire M, Radcliffe A. Mechanical palpation for subsurface sensing: A device for detecting and locating breast cancer. Proc. IEEE Annu. Northeast Bioeng. Conf. NEBEC 2014;2014–Decem:3–4. doi: 10.1109/NEBEC.2014.6972743.

6. Kennedy KM, Chin L, McLaughlin RA, Latham B, Saunders CM, Sampson DD, Kennedy BF. Quantitative micro-elastography: imaging of tissue elasticity using compression optical coherence elastography. Sci. Rep. [Internet] 2015;5:15538. doi: 10.1038/srep15538.

7. Venkatesh SK, Yin M, Ehman RL. Magnetic resonance elastography of liver: technique, analysis, and clinical applications. J. Magn. Reson. Imaging [Internet] 2013;37:544–55. doi: 10.1002/jmri.23731.

8. Yamakoshi Y, Sato J, Sato T. Ultrasonic Imaging of Internal Vibration of Soft Tissue under Forced Vibration. IEEE Trans. Ultrason. Ferroelectr. Freq. Control 1990;37:45–53. doi: 10.1109/58.46969.

9. Muthupillai R, Lomas D, Rossman P, Greenleaf J, Manduca A, Ehman R. Magnetic resonance elastography by direct visualization of propagating acoustic strain waves. Science (80-.). [Internet] 1995;269:1854–1857. doi: 10.1126/science.7569924.

10. Sinkus R, Daire JL, Van Beers BE, Vilgrain V. Elasticity reconstruction: Beyond the assumption of local homogeneity. Comptes Rendus - Mec. 2010;338:474–479. doi: 10.1016/j.crme.2010.07.014.

11. Kolipaka A, Mcgee KP, Manduca A, Romano AJ, Glaser KJ, Araoz PA, Ehman RL. Magnetic Resonance Elastography : Inversions in Bounded Media. Magn. Reson. Med. 2009;1542:1533–1542. doi: 10.1002/mrm.22144.

12. Low G. General review of magnetic resonance elastography. World J. Radiol. [Internet] 2016;8:59. doi: 10.4329/wjr.v8.i1.59.

13. Mariappan YK, Glaser KJ, Ehman RL. Magnetic Resonance Elastography: A Review. Clin. Anat. 2010;5:497–511. doi: 10.1126/scisignal.2001449.Engineering.

14. Kruse SA, Rose GH, Glaser KJ, Manduca A, Felmlee JP, Jr CRJ, Ehman RL. Magnetic resonance elastography of the brain. Neuroimage 2008;39:231–237. doi: 10.1016/j.neuroimage.2007.08.030.

15. Uribe S, Beerbaum P, Sørensen TS, Rasmusson A, Razavi R, Schaeffter T. Four-dimensional (4D) flow of the whole heart and great vessels using real-time respiratory self-gating. Magn. Reson. Med. 2009;62:984–992. doi: 10.1002/mrm.22090.

16. Feng L, Grimm R, Block KT obias, Chandarana H, Kim S, Xu J, Axel L, Sodickson DK, Otazo R. Golden-angle radial sparse parallel MRI: combination of compressed sensing, parallel imaging, and golden-angle radial sampling for fast and flexible dynamic volumetric MRI. Magn. Reson. Med. 2014;72:707–717. doi: 10.1002/mrm.24980.

17. Muthupillai R, Rossman PJ, Lomas DJ, Greenleaf JF, Riederer SJ, Ehman RL. Magnetic resonance imaging of transverse acoustic strain waves. Magn. Reson. Med. [Internet] 1996;36:266–274. doi: 10.1002/mrm.1910360214.

18. Garteiser P, Sahebjavaher RS, Ter Beek LC, Salcudean S, Vilgrain V, Van Beers BE, Sinkus R. Rapid acquisition of multifrequency, multislice and multidirectional MR elastography data with a fractionally encoded gradient echo sequence. NMR Biomed. 2013;26:1326–1335. doi: 10.1002/nbm.2958.

19. Rump J, Klatt D, Braun J, Warmuth C, Sack I. Fractional encoding of harmonic motions in MR elastography. Magn. Reson. Med. 2007;57:388–395. doi: 10.1002/mrm.21152.

20. Guenthner C, Kozerke S. Encoding and Readout Strategies in Magnetic Resonance Elastography. Zurich; Unpublished.

21. Liang D, Liu B, Wang J, Ying L. Accelerating SENSE using compressed sensing. Magn. Reson. Med. 2009;62:1574–1584. doi: 10.1002/mrm.22161.

22. Lustig M, Donoho D, Pauly JM. Sparse MRI: The application of compressed sensing for rapid MR imaging. Magn. Reson. Med. 2007;58:1182–1195. doi: 10.1002/mrm.21391.

23. Beatty PJ. Reconstruction Methods for fast MRI. Stanford; 2006.

24. Lustig, Michael and Donoho, David L and Santos, Juan M and Pauly JM. Compressed sensing MRI. Signal Process. Mag. IEEE 2008;25:72–82. doi: Doi 10.1109/Tit.2006.871582.

25. Geethanath S, Reddy R, Konar AS, Imam S, Sundaresan R, D. R. RB, Venkatesan R. Compressed Sensing MRI: A Review. Crit. Rev. Biomed. Eng. [Internet] 2013;41:183–204. doi: 10.1615/CritRevBiomedEng.2014008058.

26. Tremoulheac B, Dikaios N, Atkinson D, Arridge SR. Dynamic MR image reconstruction-separation from undersampled (k,t)-Space via low-rank plus sparse prior. IEEE Trans. Med. Imaging 2014;33:1689–1701. doi: 10.1109/TMI.2014.2321190.

27. Chandarana H, Feng L, Ream J, Wang A, Babb JS, Block KT, Sodickson DK, Otazo R. Respiratory Motion-Resolved Compressed Sensing Reconstruction of Free-Breathing Radial Acquisition for Dynamic Liver Magnetic Resonance Imaging. Invest. Radiol. [Internet] 2015;50:749–756. doi: 10.1097/RLI.0000000000000179.

28. Taubman DS, Marcellin MW. JPEG 2000: Image Compression Fundamentals, Standards and Practice. Norwell, MA, USA: Kluwer Academic Publishers; 2001.

29. Daniel Fovargue. MRE Shear Stiffness Reconstruction Software. London; Unpublished.

30. Roemer PB, Edelstein WA, Hayes CE, Souza SP, Mueller OM. The NMR phased array. Magn. Reson. Med. 1990;16:192–225. doi: 10.1002/mrm.1910160203.

31. Wundrak S, Paul J, Ulrici J, Hell E, Geibel MA, Bernhardt P, Rottbauer W, Rasche V. A self-gating method for time-resolved imaging of nonuniform motion. Magn. Reson. Med. [Internet] 2016;76:919–925. doi: 10.1002/mrm.26000.

32. Buehrer M, Curcic J, Boesiger P, Kozerke S. Prospective self-gating for simultaneous compensation of cardiac and respiratory motion. Magn. Reson. Med. 2008;60:683–690. doi: 10.1002/mrm.21697.

33. Chandarana H, Feng L, Block TK, Rosenkrantz AB, Lim RP, Babb JS, Sodickson DK, Otazo R. Free-Breathing Contrast-Enhanced Multiphase MRI of the Liver Using a Combination of Compressed Sensing, Parallel Imaging, and Golden-Angle Radial Sampling. 2013;48:1–17. doi: 10.1097/RLI.0b013e318271869c.Free-Breathing.

Appendix

The code used in reconstruction and evaluation, along with a demonstration dataset, is available under the following link:

https://polybox.ethz.ch/index.php/s/7uBTZhiaCtya6Wy (Password: MRE2017)

Additional Figures

All figures found in the work, as well as variations of Figure 8, Figure 9 and Figure 11 utilizing different quality metrics which were used in evaluation are available under the following link:

https://polybox.ethz.ch/index.php/s/EzoWPg54lluSA22

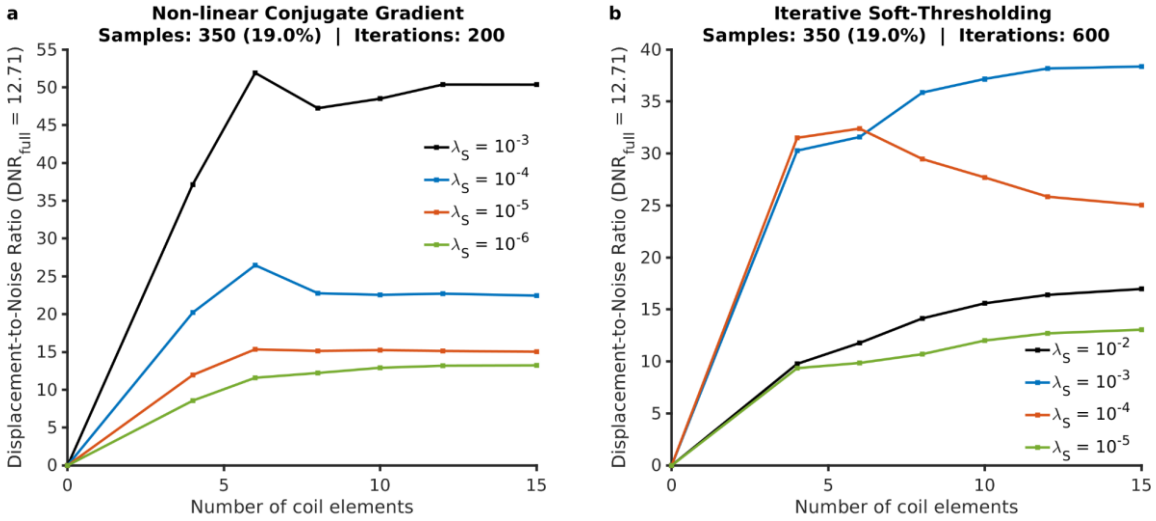

Figure 16: Relation of DNR to the number of coil elements from which reconstruction is performed. Here, a number of measured coil sensitivity maps was selected and reconstruction was performed using (a) the conjugate gradient and (b) soft-thresholding approach. Since DNR is dependent on noise levels it also correlates with Signal-to-Noise Ratio, hence it is possible to obtain lower DNR values using additional coils, if the SNR of the selected coil element contributes more less signal than noise compared to previous elements. Since reconstruction can be performed faster with fewer coil elements, it can be beneficial to use only elements with a higher SNR for image reconstruction.